Numerical simulations of the three-dimensionalization of a shear flow in radiatively forced cold water below the density maximum

Andrew P. Grace [1,*] Marek Stastna,[1] K. G. Lamb [1] and K. Andrea Scott [2]

[1]*Department of Applied Mathematics, University of Waterloo, Waterloo, Ontario N2L 3G1, Canada*
[2]*Department of Systems Design Engineering, University of Waterloo, Waterloo, Ontario N2L 3G1, Canada*

Recently the dynamics of flows beneath ice cover has garnered much interest in the environmental fluid dynamics community. Of particular importance is understanding how heat introduced via solar radiation is transported within a body of cold fresh water (characteristic temperatures are below the temperature of maximum density), and how a subsurface current affects this process. In this study we present high-resolution numerical simulations of the interaction between cold water convection and a parallel shear flow. The results of this paper show that for a sufficiently strong shear current, the growth phase of instabilities generated by volumetric thermal forcing (which represents solar radiation) is nearly two-dimensional and that the transition to more vigorous three-dimensional motion is initialized by baroclinic production of vorticity by convective instabilities followed by a rapid increase in streamwise vorticity generated by vortex tilting and stretching. We describe how this process is modified by differences in shear strength and thermal forcing attenuation length.

I. INTRODUCTION

Over the past few years, the role of wintertime fluid dynamics in ice covered lakes has gained considerable prominence in the limnological literature, thus garnering much interest from many different perspectives. Powers and Hampton [1] provides a survey of some key findings in a variety of fields of study. A recent review article by Jansen *et al.* [2] provides key interdisciplinary research questions for the emerging field of winter limnology, some proposed methods to answer these questions, and the level of field-specific expertise required to answer them. An important thread between many of the research questions mentioned in Powers and Hampton [1] and Jansen *et al.* [2] involve understanding and predicting the temporal and spatial variability of the water column as energy enters the system. Energy in the form of heat that enters the system often drives horizontal and vertical convection which in turn modify flows beneath ice. A summary of convective processes from a dynamical perspective relevant to lake scales can be found in Bouffard and Wüest [3], and a more directed summary on physical processes beneath lake ice can be found in Kirillin *et al.* [4].

A primary discussion point of Bouffard and Wüest [3] and Kirillin *et al.* [4] is that convection beneath ice is responsible for a host of processes, that have wide ranging implications for both the present and future states of the water column. For instance, Yang *et al.* [5,6] showed that overturning generated by vertical convection may have serious implication for dissolved oxygen concentrations for the subsequent spring in Lake Simcoe, Canada. Cortés and MacIntyre [7] showed that nonlinear internal waves occurred beneath ice in an arctic lake and this led to considerable mixing of the water column during ice-off, and horizontal convection had a significant role in the offshore transport of

---

*andrew.grace@uwaterloo.ca
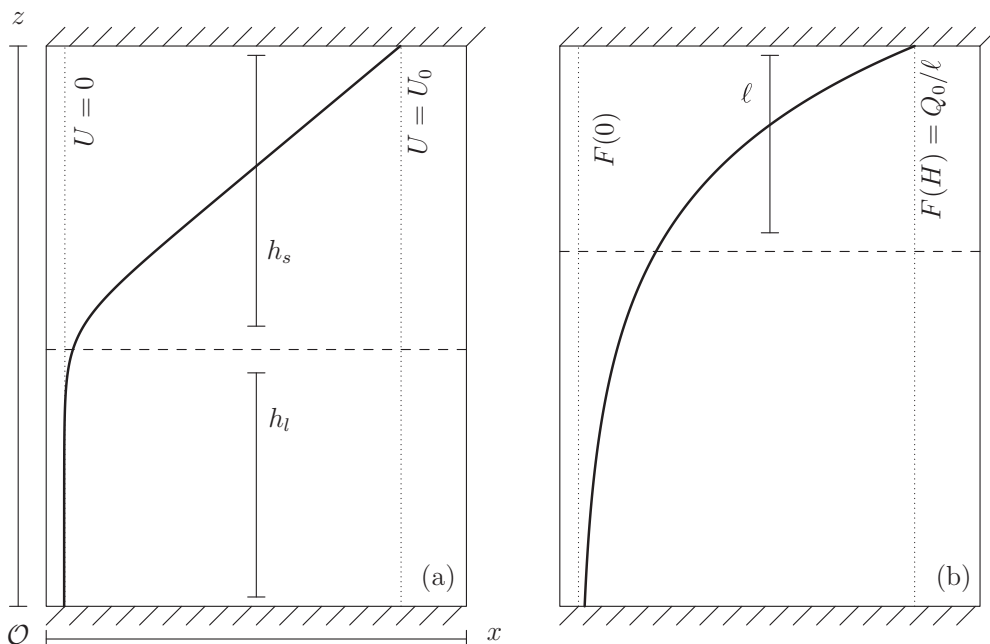
FIG. 1. (a) The background velocity profile from equation (7). The maximum upper layer velocity is U_0. The upper layer depth is h_s, and the lower layer depth is h_l. The thermal forcing profile is shown in panel (b). The decay scale of the thermal forcing is ℓ, and the magnitude at the surface is Q_0. One e-folding scale is located at a height $H - \ell$.

oxygen. Ramón *et al.* [8] simulated a small lake subjected to incident solar radiation to describe the roles that the Rossby number and lake bathymetry play in the lateral heat distribution by horizontal convection. For the same lake dimensions, Ulloa *et al.* [9] showed that lateral flows generated by differential heating must be accounted for in order to accurately determine mixed layer depth beneath ice.

During ice-covered seasons, the primary mechanism responsible for introducing energy into the water column is solar radiation. Some of that radiation is reflected or absorbed by the ice, and some of it penetrates into the underlying water column, with its intensity decreasing approximately exponentially with depth. The rate at which the intensity of the radiation is attenuated with depth is encoded in an attenuation length scale that is a function of both the clarity of the water and the wavelength of the incident radiation. Smaller attenuation lengths represent more absorption near the ice-water surface, and larger attenuation lengths represent penetration to greater depths.

Owing to the fact that freshwater temperatures beneath ice are typically below the temperature of maximum density (3.98 °C), the added heat that increases the temperature of the water also increases its density. Since the bulk of the heat is added near the surface, solar radiation ultimately leads to the formation of an unstable stratification that induces overturning and subsequent homogenization of the water column. Yang *et al.* [5] used thermistor chain data in Lake Simcoe, Canada, to show homogenization of the water column due to overturning once the snow on the ice surface had melted (their Fig. 2). This result provides practical evidence of total homogenization by convection driven by solar radiation. Part of the uniqueness of the cold water regime is that characteristic density differences ($\Delta\rho = \rho_1 - \rho_2$) within the flow are very small. The density differences within a flow are usually characterized by the Atwood number, At $= (\rho_1 - \rho_2)/(\rho_1 + \rho_2)$ [10]. There has been some interest in mixing in small At flows. Andrews and Dalziel [10], Boffetta *et al.* [11,12] and Akula *et al.* [13] quote At in the range of $O(0.01)$–$O(0.1)$ but it can be much smaller in other
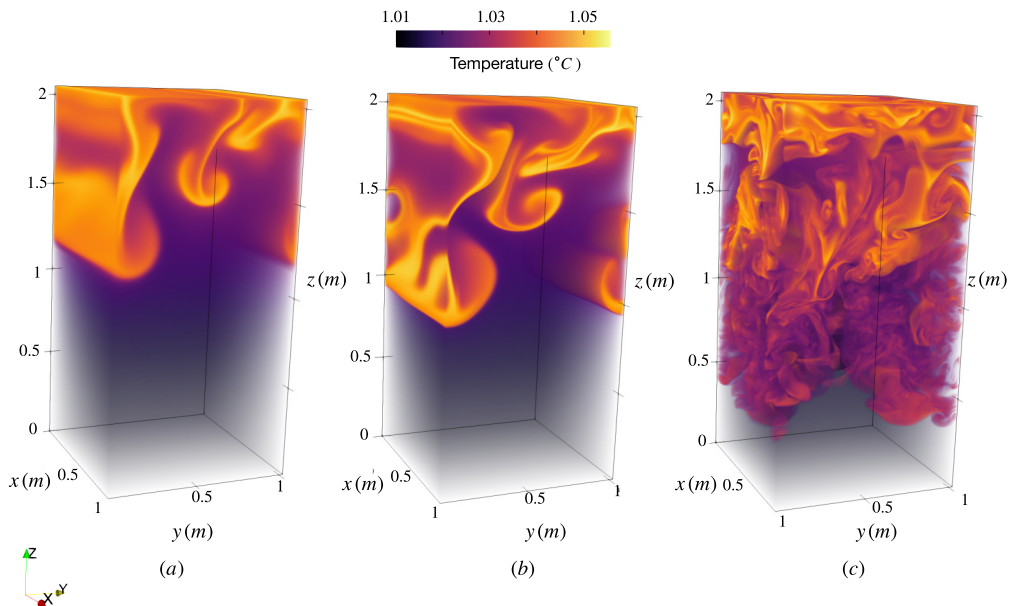
FIG. 2. Three-dimensional renderings of the temperature field for the Fast case during the instability growth phase (a, b) and after full collapse of the water column (c). Panel (a) is at 3600 s, panel (b) at 3800 s, and panel (c) at 4300 s. The background current is directed along the x axis (indicated by the orientation axes in the bottom left corner). Higher temperatures correspond to higher opacity.

applications. For example, based on the initial and final state considered in this study, At is in the range of $O(10^{-5})$.

The process of overturning generated by solar radiation is complicated by the presence of subsurface currents. For instance, there is evidence of very slow (several mm/s) subsurface currents beneath ice cover in Lake Vendyurskoe (Russia) [14], induced by a unimodal seiche. More vigorous subsurface (several cm/s) currents can occur as a result of under ice river plumes as well. In simulations of an under-ice river plume, Kasper and Weingartner [15] showed that velocities were in the range of less than 5–10 cm/s beneath ice cover. The discharge that they used was representative of the spring freshet of a small arctic river. This order of magnitude agrees with measurements of the flows beneath landfast ice in the Alaskan Beaufort Sea by Weingartner *et al.* [16]. There is considerable theoretical evidence showing that the development of the convective instabilities is coupled to the shear generated by flows like those beneath ice cover.

Benilov *et al.* [17] used a jet velocity profile and a quasi-two-layer inverse stratification to show that near the tip of the jet (where the vertical shear is near zero), Rayleigh-Taylor instabilities (RTIs) occurred, but on the flanks of the jet (where the vertical shear is increasing or decreasing), no RTIs were noted. They followed this with a numerical study that showed that by increasing the magnitude of homogeneous shear, the width of the unstable region in spectral space decreased but stayed finite. Furthermore, the growth rates always had an interior peak, indicating that there is always a single fastest growing instability. Their conclusion was that streamwise instabilities will always occur in their system and the length scale of the primary instability is proportional in some way to the magnitude of the shear.

Mikhailenko *et al.* [18] went a step further and showed that streamwise RTIs are suppressed in regions where

$$|U_z(z)| \geqslant \frac{\sigma_i}{\sqrt{2}}. \tag{1}$$

Here $|U_z|$ is the local magnitude of the shear, and σ_i is the growth rate of the fastest growing instability in the absence of any background shear. While the result of Mikhailenko *et al.* [18] is mathematically sound, the theory does not include a spanwise dimension. Multiple studies in varying convection contexts have shown that shear interacting with an unstable stratification in three dimensions leads to rollers with their cores aligned with the background current. Kuo [19] commented that cloud streets occur because of the suppression of streamwise instability, leaving spanwise perturbations to grow. Keisuke *et al.* [20] noted that the interaction between Rayleigh-Bénard convection and shear in their experiments on coherent turbulent structures led to the formation of rollers. Finally, Pirozzoli *et al.* [21] showed these rollers in a similar setup using numerical simulations for a variety of Reynolds numbers and Rayleigh numbers. To our knowledge, no numerical studies on cold water convection induced by volumetric thermal forcing interacting with shear have been carried out.

In this article, we study the interaction between a shear flow and convection induced by nonuniform heating in cold water. Heat is continually added such that an unstable density gradient is created near the surface giving rise to convective instabilities. We investigate the development of the instabilities and the transition to turbulence using high resolution three-dimensional simulations. We discuss with examples the roles that the magnitude of the shear and the attenuation length scale play in the transition to turbulence. In this study, the word "turbulence" is used to describe the random and chaotic flow state, and is used in the qualitative sense. A directed discussion on the turbulent state will be pursued in future work.

The structure of the article is as follows. First we describe the numerical model, the equations of motion, and the setup we are modeling. Then we show the results highlighting the instability development and the transition to turbulence. The last section provides a summary and discussion of the results, as well as a description of the limitations of simulating this system in two dimensions. We conclude with future research directions.

II. PROBLEM FORMULATION

The study presented in this paper is motivated by under-ice dynamics as a result of heat deposition in lacustrine bodies over the winter. In a complete lacustrine system, many competing mechanisms and processes must be included to properly represent the full range of dynamics. However, the specific modeling choices presented herein are meant to represent experimental scales, thus maximizing the capabilities of our numerical model (discussed below). Pursuant to this, the conceptual model presented below is simplified in order to have a properly constrained study.

In this study we use the pseudospectral numerical model SPINS [22] to perform direct numerical simulations of the incompressible Navier-Stokes equations under the Boussinesq approximation to model the interaction between cold water (temperatures between $0\,°C$ and the freshwater temperature of maximum density) convection generated by volumetric thermal forcing and a shear current in a rectangular domain of length and width L (ranges from 1.024 to 2.048 m) and depth H (2.048 m). We adopt the standard oceanographic coordinate system so that the streamwise (direction of the shear current), spanwise, and vertical (positive upwards) directions are denoted by (x, y, z), respectively, and corresponding unit vectors $\hat{\boldsymbol{i}}$, $\hat{\boldsymbol{j}}$, and $\hat{\boldsymbol{k}}$. The boundary conditions for the top and bottom surfaces are free-slip for velocity and no-flux for temperature, while the boundary conditions are periodic in the horizontal directions. The uniform grid spacing is $(\Delta x, \Delta y, \Delta z) = (4 \times 10^{-3}, 4 \times 10^{-3}, 2 \times 10^{-3})$ m, respectively. A resolution sensitivity test was performed on the Slow-Narrow case (Table II) and revealed that the instability development was insensitive to higher resolutions, thus, the resolution was selected to balance accuracy and expediency of simulation. A domain size test was also performed and the domain size presented herein is sufficient to resolve the scales of interest.

In the simulations in this study, the temperature is an initially uniform value of T_0 (Table I), chosen to be less than the temperature of maximum density for freshwater, T_{md}. The choice of a uniform temperature is made to simplify the modeling approach. Ulloa *et al.* [9] and Ramón *et al.* [8]

TABLE I. Constants used in this paper. g is gravity, ρ_{md} is the constant background density, C is the fitting constant for the equation of state, H is the depth of the domain, ν is the kinematic viscosity, κ is the diffusivity, T_0 is the initial temperature, and Q_0 is the magnitude of the thermal forcing. L is found in Table II.

g (m/s^2)	ρ_{md} (kg/m^3)	C (°C^{-2})	T_{md} (°C)	H (m)	ν (m^2/s)	κ (m^2/s)	T_0 (°C)	Q_0 (°C m/s)
9.81	999.97	7.6×10^{-6}	3.98	2.048	10^{-6}	10^{-7}	1	7.25×10^{-6}

observed a cross-shore shear flow within the convective mixed layer in their simulations indicating some numerical evidence for the coexistence of a shear flow in a uniform temperature environment. The equations of motion that are solved by the model are

$$\frac{D\boldsymbol{u}}{Dt} = -\frac{1}{\rho_{md}}\boldsymbol{\nabla}p - g\rho\hat{\boldsymbol{k}} + \nu\nabla^2\boldsymbol{u}, \tag{2}$$

$$\frac{DT}{Dt} = \kappa\nabla^2 T + F(z), \tag{3}$$

$$\boldsymbol{\nabla}\cdot\boldsymbol{u} = 0. \tag{4}$$

The material derivative is represented by $\frac{D}{Dt} = \frac{\partial}{\partial t} + \boldsymbol{u}\cdot\boldsymbol{\nabla}$, the three-dimensional velocity is given by $\boldsymbol{u}$, time is given by t, pressure is given by p. Viscosity is given by ν, the temperature diffusivity by κ, and g is the gravitational acceleration, all of which are found in Table I. $\rho(T)$ is the density perturbation about the reference density ρ_{md}. The nonlinear equation of state used in this study is

$$\rho = -C(T - T_{md})^2, \tag{5}$$

where $T(x, y, z, t)$ is the temperature field, and the value of the constant C is given in Table I. Equation (5) is a quadratic fit to the equation of state in McDougall et al. [23] and is valid for freshwater between 0 °C and 10 °C. Since the temperatures attained in the study do not deviate very far from 1 °C (the initial temperature), this is an adequate approximation. A similar equation of state was used to study the development of Rayleigh-Taylor instability (RTI) from a finite thickness interface in cold water in Olsthoorn et al. [24].

The volumetric heating is represented by $F(z)$ [°C/s] and an example profile is shown in Fig. 1(b) and is a simple model of penetrative short wave radiation. The forcing takes the form of an exponential with a single decay scale and is called the Beer-Lambert Law. Mathematically, it is given by

$$F(z) = \frac{Q_0}{\ell}\exp\left(\frac{z - H}{\ell}\right). \tag{6}$$

Two important parameters appear in this formulation of the forcing. They are Q_0, the magnitude of the thermal forcing at the top of the domain, and ℓ, the attenuation length.

The value for Q_0 used throughout the manuscript is found in Table I, and corresponds to an intensity of approximately 30 W/m^2 when multiplied by $\rho_0 c_p$. This value is an order of magnitude estimate for the intensity of radiation that penetrates beneath a representative amount of snow and ice cover on a natural body of water in the late winter [4,9].

The attenuation length, ℓ, is provided in Table II for each case. The attenuation length controls how fast the incoming radiation is attenuated with depth and is a function of both the water's clarity and the frequency of the incident radiation. The Jerlov water-type system presents a basis for categorizing water based on its clarity and assigns attenuation length scales based on how certain frequency bands of light are absorbed for a given turbidity [25]. Common parametrizations of penetrative shortwave radiation often contain more than one forcing component, each with its own associated attenuation length. Including multiple absorption bands may be necessary for adequately representing mechanisms such as photosynthesis, gas dynamics, or stratification development

TABLE II. Cases considered in this paper. U_0 is the maximum velocity of the background current, L is the streamwise length of the tank (equal to the spanwise length of the tank for all cases), ℓ is the attenuation length of the thermal forcing, and $N_x \times N_y \times N_z$ is the grid resolution.

Case	U_0 (m/s)	L (m)	ℓ (m)	$N_x \times N_y \times N_z$ —
Base	0	1.024	0.6	$256 \times 256 \times 1024$
Slow	0.001	1.024	0.6	$256 \times 256 \times 1024$
Fast	0.01	1.024	0.6	$256 \times 256 \times 1024$
Fast-Wide	0.01	2.048	0.6	$512 \times 512 \times 1024$
Fast-Narrow	0.01	0.512	0.6	$128 \times 128 \times 1024$
Medium-Attenuation	0.01	1.024	0.4	$256 \times 256 \times 1024$
Short-Attenuation	0.01	1.024	0.2	$256 \times 256 \times 1024$
Short-Attenuation-Wide	0.01	2.048	0.2	$512 \times 512 \times 1024$

[26,27]. For reference, other established codes like the MITgcm [28], and ELCOM [27] use two- and three-band models respectively in their default setups. The columnar model used in Simpson and Dickey [29] and Simpson and Dickey [26] used up to 10 bands for some experiments.

Since this study is not concerned with the precise distribution of heat by the solar radiation, and is instead concerned with the redistribution of heat by instabilities generated by the unstable stratification, we follow the approach of Ulloa *et al.* [9] and Bouffard and Wüest [3] and parametrize the incident radiation as a single-band model. In the context of cold water, Bouffard and Wüest [3] simplified the Jerlov system and made an order of magnitude estimate that attenuation lengths for clear water beneath ice are $O(1 \text{ m})$ and for turbid water beneath ice are $O(0.1 \text{ m})$.

The value for ℓ in the Base case (Table II) was initially chosen to be similar in magnitude to the attenuation length used in Ulloa *et al.* [9], who used $\ell = 0.4$ m. For cases where ℓ was changed from the value in the Base case, the value was chosen such that there were clear differences in dynamics but was also in the neighborhood of the turbid estimate from Bouffard and Wüest [3].

In all cases, we should expect convective instabilities to grow at a rate proportional to two quantities: (1) the density difference between consecutive fluid layers, often quantified by the Atwood number (see the Introduction) and (2) how much energy is initially present in each wave number. The initial energy in each wave number is controlled by the size of the initial white noise perturbation. Each simulation presented is seeded with a velocity perturbation of $u_{pert} = 10^{-6}$ m/s, the magnitude of which is held constant across all cases.

Finally, the velocity profile (current will be used interchangeably) considered for this study has a layer of constant shear atop a layer with no background velocity. Measurements of the velocity profiles in the near-mouth region of small river plumes [30] indicate nearly piecewise linear velocity profiles. The form of the current used in this study is given by

$$U(z) = \frac{U_0}{H} \int_0^z \left[1 + \tanh\left(\frac{z' - \frac{1}{2}H}{\delta} \right) \right] dz',$$ (7)

and is shown schematically in Fig. 1(a). Here δ controls how rapidly the profile transitions from motionless to the constant shear state. This parameter is held constant across all simulations at 0.1 m. Values for H and U_0 (the depth of the domain and maximum velocity of the current) are found in Tables I and II, respectively. A key feature about the profile in Eq. (7) is that it initially precludes the formation of shear instabilities by Rayleigh's inflection point criterion [31]. Shear instabilities provide a means for column wide mixing but are not of interest here.

III. VORTICITY DIAGNOSTICS

The main goal of this study is to examine how the system moves from a quasi-two-dimensional state to a fully three-dimensional state, and what role the attenuation length and the magnitude of the shear play in that process. A simple way to establish when the flow goes fully three-dimensional is to examine the vorticity components,

$$\boldsymbol{\omega} = \boldsymbol{\nabla} \times \boldsymbol{u}, \tag{8}$$

as well as the enstrophy,

$$\tfrac{1}{2}|\boldsymbol{\omega}|^2 = \tfrac{1}{2}\left(\omega_x^2 + \omega_y^2 + \omega_z^2\right), \tag{9}$$

where $\boldsymbol{\omega} = (\omega_x, \omega_y, \omega_z)$ (subscripts indicate direction in this context). For brevity, enstrophy components normalized by the total enstrophy are denoted as

$$\left(\tilde{\omega}_x^2, \tilde{\omega}_y^2, \tilde{\omega}_z^2\right) = \frac{\left(\omega_x^2, \omega_y^2, \omega_z^2\right)}{|\boldsymbol{\omega}|^2}. \tag{10}$$

A characteristic of three-dimensional fluid flow is that vorticity vectors typically have three nonzero components, while in two-dimensional flow, there is only one nonzero component. Thus, to determine when and under what conditions the streamwise symmetry of the flow breaks, we can first look at how the vorticity components change over time.

We can take the curl of the momentum equations to get a system of vorticity equations

$$\frac{D\omega_x}{Dt} = \nu\nabla^2\omega_x - g\frac{\partial\rho}{\partial y} + \boldsymbol{\omega}\cdot\boldsymbol{\nabla}u, \tag{11}$$

$$\frac{D\omega_y}{Dt} = \nu\nabla^2\omega_y + g\frac{\partial\rho}{\partial x} + \boldsymbol{\omega}\cdot\boldsymbol{\nabla}v, \tag{12}$$

$$\frac{D\omega_z}{Dt} = \nu\nabla^2\omega_z + \boldsymbol{\omega}\cdot\boldsymbol{\nabla}w. \tag{13}$$

The terms on the right-hand side of each of the above equations are responsible for the net changes in vorticity. The Laplacian (∇^2) terms diffuse vorticity in regions of high spatial variation, but will be ignored in the following analysis. The remaining terms are the baroclinic generation terms $(-g\frac{\partial\rho}{\partial y})$ and $(g\frac{\partial\rho}{\partial x})$, and the vortex tilting/stretching terms $\boldsymbol{\omega}\cdot\boldsymbol{\nabla}u$. Next, two metrics called S_i and B_i are defined as

$$S_i = \sqrt{\iint |\omega_j\partial_j u_i|^2\, dx_1\, dx_2}, \tag{14}$$

$$B_i = g\sqrt{\iint |\epsilon_{ij3}\partial_j\rho_3|^2\, dx_1\, dx_2}. \tag{15}$$

S_i and B_i are the horizontal L^2 norms of the tilting/stretching terms and baroclinic generation terms for the ith component of vorticity ($i = 1, 2, 3$), respectively. Note that $B_3 = 0$. These metrics allow us to compare the strengths of the vortex stretching/tilting and baroclinic terms in Eqs. (11)–(13) at every vertical level in the domain.

IV. NUMERICAL EXPERIMENTAL DESIGN

Table I shows the parameters held constant across all simulations, and Table II shows the parameters that are varied. The results presented below are broken up into two subsections. The first describes the instability growth phase, and the second describes the transition to a turbulent state.

The first subsection is broken down further into separate sections that describe the roles the shear layer and the attenuation length play. The role that the shear layer plays in that process is described through comparison of the Base, Slow, and Fast cases. These cases are chosen because they show three different behaviors based on the magnitude of the shear flow. The Base case shows one extreme where there is no shear flow, and the system evolves under only the volumetric thermal forcing. The Slow case presents an example where there is a background shear flow, but it is not strong enough to suppress the streamwise variation in the instability growth. Finally, the Fast case provides an example where the shear flow can temporarily prevent the streamwise variation in the instability growth. The role that the attenuation length plays in the instability growth is discussed after, with reference to the Fast, Medium-Attenuation, and Short-Attenuation cases. These cases demonstrate how changing the attenuation length changes key aspects of the instability growth and eventual destabilization.

The second section describes the transition to the full three-dimensional state and cases are compared as necessary.

From the parameters listed in Tables I and II we can use dimensional analysis to define a convective velocity scale $\mathcal{U}$, and a temperature scale θ as

$$\mathcal{U} = (Cg\ell\Delta T Q_0)^{1/3}, \quad \theta = \left(\frac{Q_0^2}{Cg\ell\Delta T}\right)^{1/3}. \tag{16}$$

$\mathcal{U}$ represents the velocity scale induced by the density differences within the flow, and ignores viscosity. θ represents the scale of the temperature anomaly about the domain averaged temperature. The domain averaged temperature depends on how long the thermal forcing has been warming the water. Last, $\Delta T = T_{md} - T_0$. Using these scalings, we can nondimensionalize the system allowing us to define the following set of parameters:

$$\text{Gr} = \left(\frac{\mathcal{U}\ell}{\nu}\right)^2, \quad \mu_1 = \frac{\ell}{H}, \quad \mu_2 = \frac{\ell}{L}, \quad \mu_3 = \frac{\delta}{\ell}, \quad \text{Pr} = \frac{\nu}{\kappa}, \quad \Theta = \frac{\theta}{\Delta T}, \quad \text{Re} = \frac{U_0 H}{\nu}. \tag{17}$$

The numbers that appear in the nondimensionalized equations are the Grashof number, Gr, the nondimensional attenuation length μ_1, the Prandtl number Pr, the nonlinear equation of state parameter, Θ, and the Reynolds number Re. The parameters μ_2 and μ_3 arise due to the boundary conditions and initial conditions respectively. Their influence on the dynamics will not be discussed. Note that in the Base case, the Reynolds number and μ_3 are not defined and are therefore not control parameters.

In this study, the Grashof number is defined as

$$\text{Gr} = \frac{(Cg\Delta T Q_0)^{2/3}\ell^{8/3}}{\nu^2} \tag{18}$$

and is a measure of the relative strengths of buoyancy and diffusion. It is a common nondimensional parameter in a variety of density-driven flow contexts. Often the Rayleigh number is used to characterize the flows in natural convection contexts (for example, see Grossmann and Lohse [32] for an exhaustive list of different scaling laws for specific contexts), but it can be shown that the Grashof number is related to the Rayleigh number through the Prandtl number. For the cases presented in this paper, $\text{Gr} = O(10^4)$–$O(10^5)$. The variation in Grashof number is achieved through the variation of ℓ.

The nonlinear parameter Θ represents the ratio of internal temperature differences to the difference between the average temperature and the temperature of maximum density, ΔT. When the internal temperature scale θ is much smaller than the bulk temperature difference ($\Theta \ll 1$), then the nonlinearity of the equation of state will have a relatively weak influence on the dynamics. Alternatively, when θ is comparable to the bulk temperature difference, then nonlinear terms in the equation of state are comparable to the linear term. In the cases presented in this paper, $\Theta \sim O(10^{-5})$, so nonlinear equation of state effects can be safely ignored.

The Prandtl number is simply the ratio of viscosity and diffusivity and is held constant across all simulations at a value of 10. This value is representative for flows with temperatures near T_{md}. In reality, the viscosity and thermal diffusivity are very weak functions of the temperature, but such dependence is ignored here.

The nondimensional attenuation length scale is represented by μ_1. In the simulations presented within, the nondimensional attenuation lengths are in the range of about 0.1 for the Short-Attenuation cases to 0.3 for the Fast and Base cases. This parameter has been studied in a context similar to the one presented here. Bouillaut *et al.* [33] performed an experimental convection study where they shined intense light on a box of fresh warm dyed water from below. The dyed water had a predictable decay scale, ℓ and they controlled μ_1 by varying the depth of water in the tank. The stated goal of the study was to show experimentally that volumetric thermal forcing achieves the so-called "ultimate regime of convection." In this regime the Nusselt number (the nondimensional vertical heat flux) scales with the square root of the Rayleigh number. They found that as μ_1 increased, the vertical heat flux became more efficient, nearly achieving the theoretical scaling law $Nu \sim Ra^{1/2}$ (the "ultimate regime" of convection). Conversely, as μ_1 was decreased, the heat flux was reduced to the traditional scaling $Nu \sim Ra^{1/3}$. The stated range of Bouillaut *et al.* [33] was $\mu_1 = 0.0015$–0.096.

Finally, the Reynolds number is the measure of the influence of inertia effects versus viscous effects. Reynolds numbers in this study vary between about $O(10^3)$–$O(10^4)$, and are manipulated via the background current speed. In studies of mixed convection, both the Grashof number and the Reynolds number appear in the equations, and their ratio Gr/Re^2 becomes important in determining the dominant balance in the flow. When $Gr \gg Re^2$, free convection is the dominant heat transfer mechanism, and heat moved by mechanical effects, like a background current or pressure gradient, becomes secondary. In the opposite case, $Gr \ll Re^2$, forced convection becomes the dominant heat transfer mechanism, meaning buoyancy driven currents are secondary to mechanical ones. Pirozzoli *et al.* [21] provides a recent study on mixed turbulent convection and the role the ratio Gr/Re^2 plays in the dynamics.

V. RESULTS

Simulations are initialized with a uniform temperature ($1\,^\circ$C), and are then thermally forced using the Beer-Lambert law. This generates an unstable background density profile. Figure 2 shows the temperature field at three times throughout the evolution of the Fast case. In this figure, the background current flows along the x direction (approximately out of the page). Figures 2(a) and 2(b) show the evolution during the instability growth phase, and Fig. 2(c) shows the water column once the instabilities have collapsed into a fully three-dimensional state. Note that fluid with temperatures near $1\,^\circ$C is rendered as nearly transparent, while fluid near $1.05\,^\circ$C (the approximate maximum across the three panels) is rendered as more opaque. Figure 2 is one example of a case that exhibits temporary quasi-two-dimensional instability growth, and this is followed by a rapid collapse to a complex three-dimensional turbulent state. The following sections describe the instability growth and transition to turbulence under different background and forcing conditions.

A. Instability growth phase

Both the magnitude of background shear flow, U_z, and the attenuation length of the thermal forcing, ℓ, play different roles in setting the growth rate and critical wave number of the instability as well as controlling the eventual destabilization of the water column. These two parameters will be discussed separately.

1. The role of the background shear flow, U_z

During the instability growth phase, the magnitude of the background shear controls whether or not the initial instability formation occurs with or without a preferential direction in the horizontal plane. Of the cases considered in Table II, only the Slow and the Base case exhibit randomly seeded
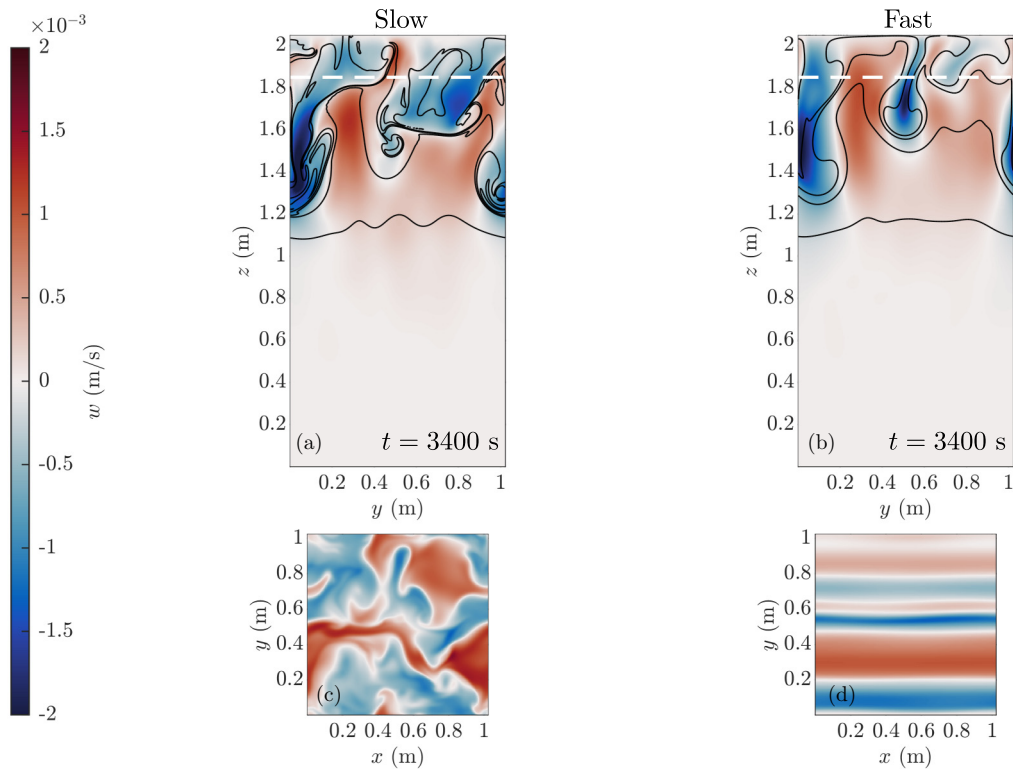
FIG. 3. A comparison of the w fields for the Slow and Fast cases. The times are on the figure. y-z slices of the Slow and Fast cases are shown in panels (a) and (b). x-z slices at the same times are shown for both cases in panels (c) and (d). The height that the x-z slice is taken at is indicated by the white dashed line in panels (a) and (b). The y-z slices are taken in the middle of the domain.

instabilities, whereas every other case exhibits instabilities aligning themselves with the background shear flow. A comparison of the Fast and Slow cases in Fig. 3 highlights the basic role that the shear flow plays as the convective plumes grow. Figures 3(a) and 3(c) show y-z and x-z slices of w for the Slow case, while Figs. 3(b) and 3(d) show the same slices of w for the Fast case. Both y-z slices have temperature contours overlaid in black. The y-z slice is taken in the middle of the domain and the white dashed line in Figs. 3(a) and 3(c) indicate the heights at which the x-y slices are taken. In Figs. 3(a) and 3(c), the direction of the background current is out of the page, while in Figs. 3(b) and 3(d) it is from left to right. The dimensional times of the plots are in the figure. Note that since the intensity of the radiation is constant in every case, plots taken at the same dimensional time have had the same amount of thermal energy added.

As the Slow case develops, the instability caused by the unstable stratification generates regions of upwelling and downwelling near the surface, but the convective plumes that form do not orient themselves either as parallel or perpendicular to the background current. The Fast case, on the other hand, exhibits a strong and persistent streamwise homogeneity until full three-dimensionalization (discussed in the next section). It is interesting to note that the magnitude of the vertical velocity is the same for both of the panels shown, even though the magnitude of the background current varies by an order of magnitude between them. This suggests that the vertical currents induced during the instability growth phase are mostly independent of the background current, thus being solely influenced by the thermal forcing. This is confirmed by calculating the vertical buoyancy flux $\langle -g\rho w \rangle$ for the Fast, Short-Attenuation, and Base cases and noting they are all on the same

order of magnitude (not shown). There is some field evidence for this. Bouffard *et al.* [34] estimated convective velocities over the course of March 2017 in Lake Onego (Russia), and the variation in daily maximums was very small, indicating that there could be an independence of the convective velocity scales from other under-ice flow factors.

2. The role of the attenuation length, ℓ

The role of ℓ is to control the rate at which incident radiation is attenuated with depth. The rate that energy is attenuated influences the size of the convective instabilities that grow. Given a constant rate at which energy is introduced by the thermal forcing, smaller values for ℓ force this energy to be concentrated over a smaller depth range thus leading to larger density differences. We can see the effect that the variation in attenuation length has on the instabilities by solving the viscous Taylor-Goldstein (vTG) equations (Appendix A) [35].

For cases when the shear is sufficiently strong so as to orient the instability cores in the streamwise direction (as in the Fast case), we solve for growth rates of perturbations in the *y-z* plane only. We make this assumption to facilitate a clearer comparison between growth curves for cases with different attenuation lengths. This decision is motivated by solving the vTG equations assuming that perturbations in any direction can grow (not shown), and noting that the maximum growth rate is found to lie along the $k = 0$ (streamwise wave number) boundary. This limit allows us to consider perturbations with only spanwise structure. Since the streamwise background current does not have any structure in the spanwise direction, it does not play a part in determining the stability of modes in the spanwise direction, and is not included in the model presented in Appendix A.

We solve the system using mean density profiles at times before the instabilities have significantly modified the stratification. Since heat is continuously added to the system, the maximum growth rates given by the vTG model are only an estimate, as a primary assumption of the model is a steady background state. Thus, we use the results of the linear model only as general guidelines for the understanding the instability growth, and not for a quantitative discussion.

The density profiles and growth curves are presented in Fig. 4. Figure 4(a) shows horizontally averaged density profiles at 1000 s (solid lines) and 2500 s (dashed lines) for attenuation lengths of 0.2 m (red) and 0.6 m (blue). These correspond to the attenuation lengths in the Short-Attenuation and the Fast cases respectively. Since the amount of heat added to the domain is linearly related to the time of each profile, the profiles shown at 2500 s have 2.5 times more heat added than the profiles at 1000 s. Since the equation of state is nonlinear, the density profile will not have the exact same structure as the thermal forcing, but since Θ is much less than unity in these cases, the increase in density is approximately linearly related to the increase in temperature. Pursuant to this, top-bottom density differences at the profiles at 2500 s are about 2.5 times as large as those taken at 1000 s. Thus the aspects of the density structure attributed to the nonlinear equation of state are secondary for the dynamics.

As heat is added, the resultant density profiles take on an exponential structure similar to the thermal forcing, thus gaining a vertical length scale on the order of the attenuation length. This vertical length scale should have some role to play in setting the horizontal length scales of the instabilities that grow in practice. Figure 4(b) shows the growth curves for instabilities growing on the background density profiles in Fig. 4(a). As the background state for a given attenuation length becomes more unstable as more heat is added (a comparison of curves with the same color), the peak of each growth curve shifts along the *l* (spanwise wave number) axis only slightly but its magnitude increases by roughly 50%. This means that as more heat is added to the domain, the wave number pertaining to the fastest growing instability does not significantly change, but the growth rate does. This is to be expected because heat added to the domain increases the temperature differences between overlying layers of fluid, thus increasing their local Atwood number. However, for a given time, a comparison of cases with different attenuation lengths (a comparison of curves with the same line style) reveals a significant difference in both the location of the peak of the growth curve, as well as the growth rate. This figure suggests that the shorter attenuation lengths have faster
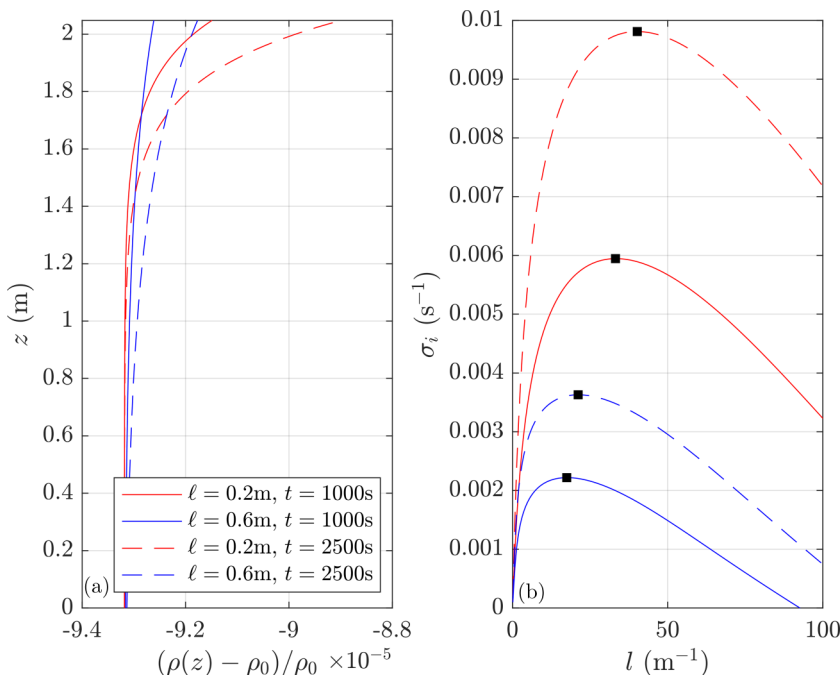
FIG. 4. (a) Three background density profiles at 1000 s (solid) and 2500 s (dashed) for the Fast and the Short-Attenuation cases. (b) The growth rates as a function of spanwise wave number (l). Note the difference in the location of the peak of the growth curve along the l axis for the different attenuation lengths. The peaks are highlighted with markers. Note also that the growth rate is larger for the shorter attenuation length.

growing instabilities with shorter characteristic length scales. This is to be expected because shorter attenuation lengths imply a larger amount of heat deposited near the surface, thus inducing a larger density gradient near the surface.

We can examine the role the attenuation length plays in practice by looking at the vertical velocities for the early development of the Short-Attenuation case at two times, shown in Fig. 5. The two main conclusions of Fig. 4(b) are qualitatively correct as smaller scale convective instabilities are observed to form much earlier in the evolution of that case relative to the Fast case. This can be seen by comparing Figs. 3(b) and 5(b), for example.

B. Transition phase

The instability growth phase focused on the early development of the instability as the system gained heat and became more unstable. The following section highlights the processes that occur as the instabilities achieve a finite amplitude, subsequently collapse and the system moves to a turbulent regime. A full discussion of the fully developed turbulent regime itself is left for future work.

As the flow develops, the streamwise symmetry (quasi-two-dimensional state) from the growth phase breaks, leading to a three-dimensional turbulent state. A qualitative appreciation of an example of the fully three-dimensional state can be seen by considering panel (c) in Fig. 2.

The full three-dimensionalization of the system will be investigated by considering the enstrophy components defined in (10).

Figure 6 shows the enstrophy components for the Fast case ($-$), Medium-Attenuation case ($--$), and Short-Attenuation case ($-\cdot$). The x, y, and z components for each case are shown in red, blue, and black. This plot can be broken into two regimes, one where the streamwise and vertical
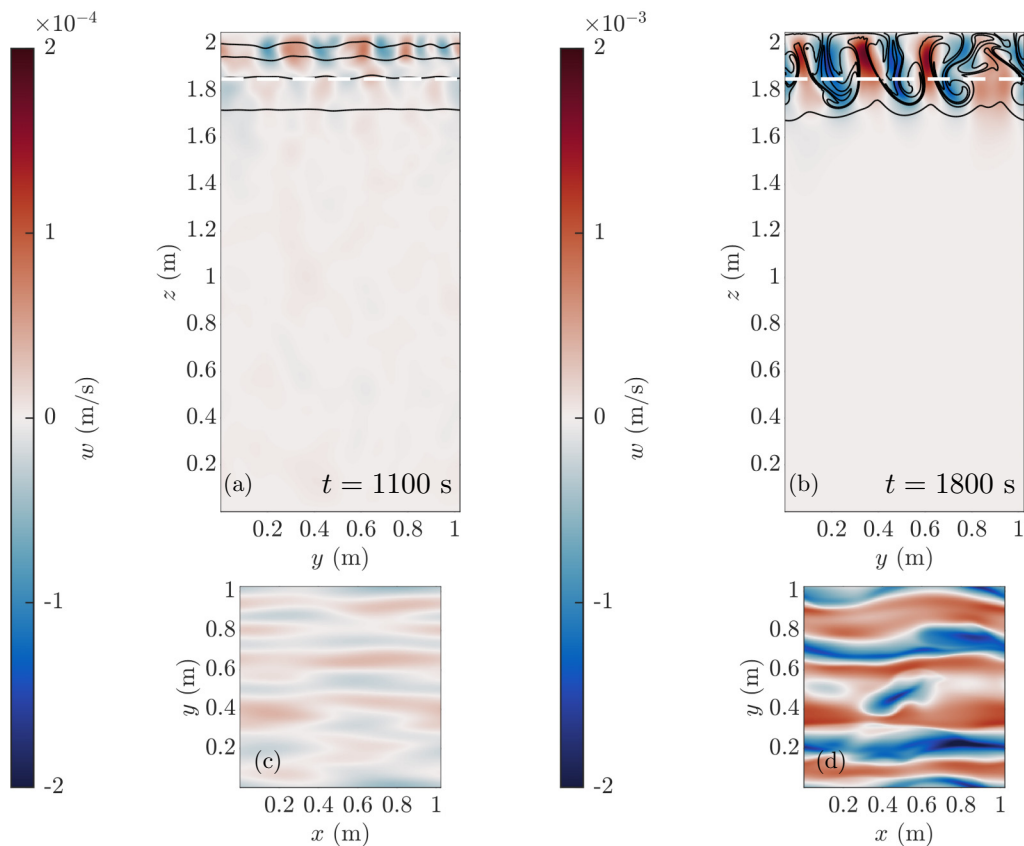
FIG. 5. A comparison of the w field at two times for the Short-Attenuation case with temperature contours overlaid. Times are chosen to highlight the initial development of the instability and the state of the instability shortly before collapse. The times are on the figure. y-z slices are shown in panels (a) and (b), and x-z slices taken at the height indicated by the white dashed line. These are shown in panels (c) and (d). Note the difference in the colorbar limits in panels (a) and (c) vs (b) and (d).

enstrophy components are distinctly different than the spanwise component, and one where they are comparable. The former corresponds to when the instability is forming and transitioning, and the latter corresponds to when the flow is strongly three-dimensional and disordered.

This plot concisely demonstrates that the system reaches a turbulent state on a shorter timescale as the attenuation length is decreased, corroborating the results in Figs. 3 and 5. Figure 6 also highlights that prior to the full three-dimensionalization, there is an increase in the streamwise and vertical components of the enstrophy, $\tilde{\omega}_x^2$ and $\tilde{\omega}_z^2$, respectively. It should be noted that significant modification of the background current occurs only after the convective plumes are very large and have had sufficient opportunity to bring momentum lower into the water column (profiles are shown in Appendix B). Thus, most of the enstrophy that is initially present is due to the background current (appearing in $\tilde{\omega}_y^2$) while the streamwise and vertical components emerge only after convective instabilities begin to modify the background state. Note that there is some initial activity in the streamwise and vertical components due to the white noise perturbation at the beginning of each simulation, but this decreases due to viscosity and the numerical filter.

As the instabilities develop and carry energy down to smaller scales with them, the net trend of the streamwise and vertical components of the enstrophy is to increase, resulting in a relative decrease of the spanwise component. This results in all three components being equal in magnitude.
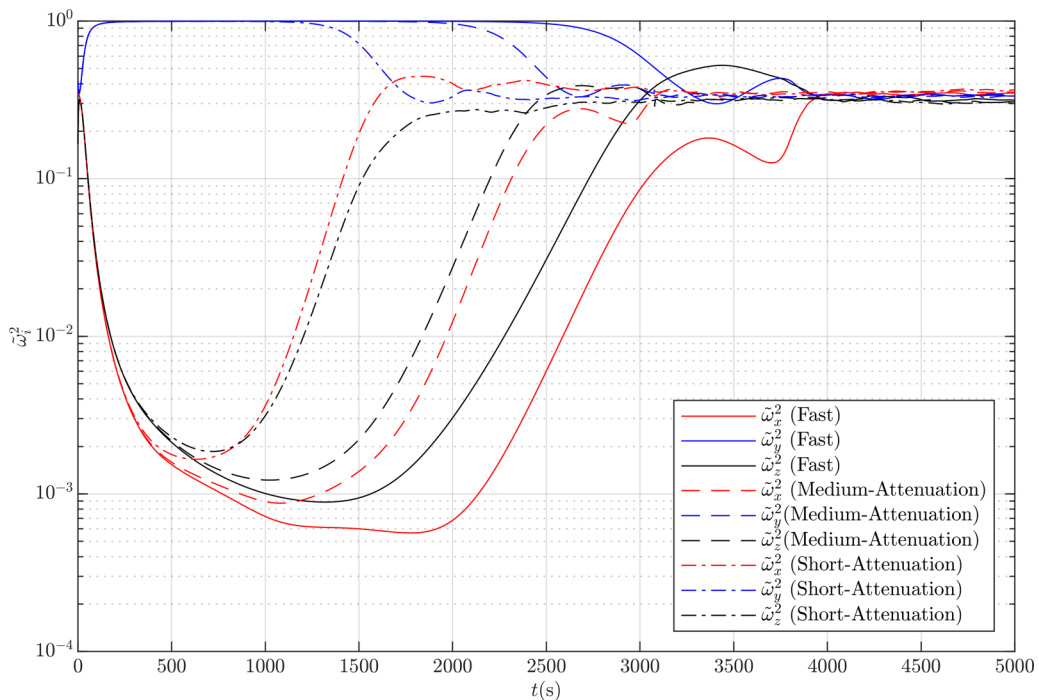
FIG. 6. Enstrophy components normalized by the total enstrophy at that time for the Fast case (solid), Medium-Attenuation case (dashed), and Short-Attenuation case (dot-dashed lines). For all cases shown, the streamwise, spanwise, and vertical components of enstrophy are red, blue, and black, respectively.

As the emergent components grow, $\tilde{\omega}_z^2$ is more active than $\tilde{\omega}_x^2$ for the Fast and Medium-Attenuation cases, and the disparity between the two is higher in the Fast case. The Short-Attenuation case is slightly different in that the streamwise component is more active than the vertical component prior to three-dimensionalization. This could arise from the fact that the instabilities grow fast enough that the shear is not able to completely suppress streamwise perturbations. This is evident in Figs. 5(c) and 5(d), as there is some streamwise variation in the vertical velocity.

Now consider Fig. 7 where we have taken the horizontal L^2 norm of each vorticity component for the Fast case. The horizontal L^2 norm is useful for assessing information regarding the vertical structure in the vorticity components. Figures 7(a)–7(c) show the norms of the streamwise, spanwise and vertical vorticity component (with vorticity of the background current removed). Coinciding with the rapid increase in spanwise vorticity in the Fast case from Fig. 6, Fig. 7(b) shows a front of strong spanwise vorticity propagating downwards. Finally, around 3900–4000 s we see larger values of streamwise vorticity near the bottom of the shear layer, which coincides with the sharp increase from Fig. 6, and the three-dimensionalization of the flow.

As the convective plumes grow and flow downwards, they bring streamwise momentum with them. The generation of spanwise and vertical vorticity occurs because of a flux of streamwise momentum from the tip and sides of the plume into the fluid moving at a different velocity below. This momentum flux manifests itself as ω_y produced at tip and ω_z produced at the sides of the plumes.

A closer look at this process is presented in Fig. 8. Shown are y-z slices of the three components of vorticity overlaid with contours of the streamwise velocity for the Fast case at 3400 s. This time was chosen because it coincides with the first local minimum of $\tilde{\omega}_y^2$ for the Fast case in Fig. 6. The Medium-Attenuation case follows the same general pattern and is not shown. Strong spanwise and vertical vorticity (Figs. 8(b) and 8(c)) are associated with strong variations in u, denoted by
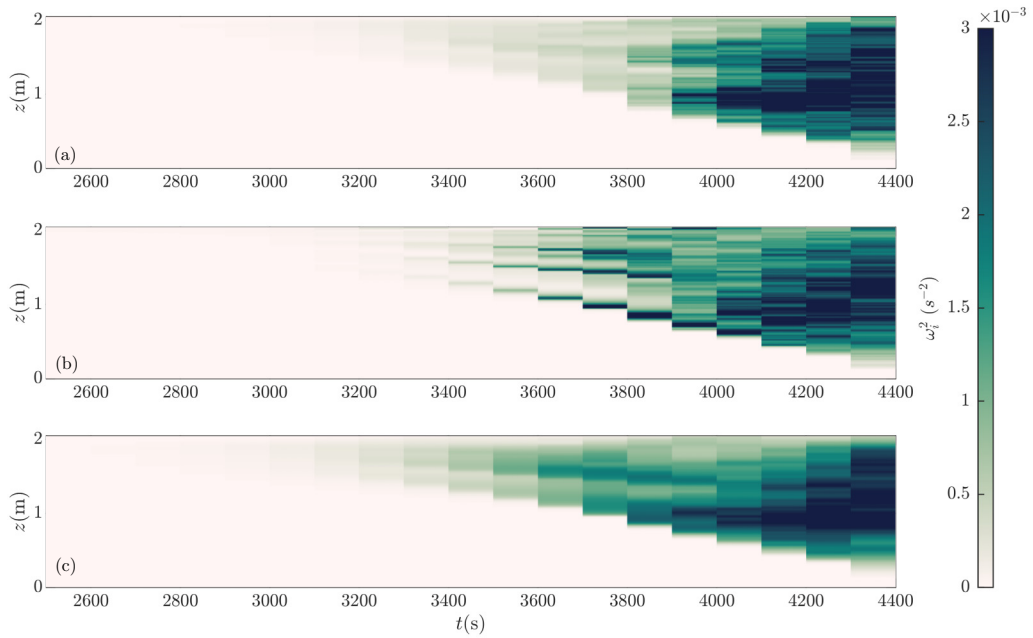
FIG. 7. Horizontal L^2 norm of the vorticity components for Fast case. (a) ω_x^2, (b) ω_y^2, and (c) ω_z^2. The vorticity contribution from the background current has been removed from ω_y before squaring.
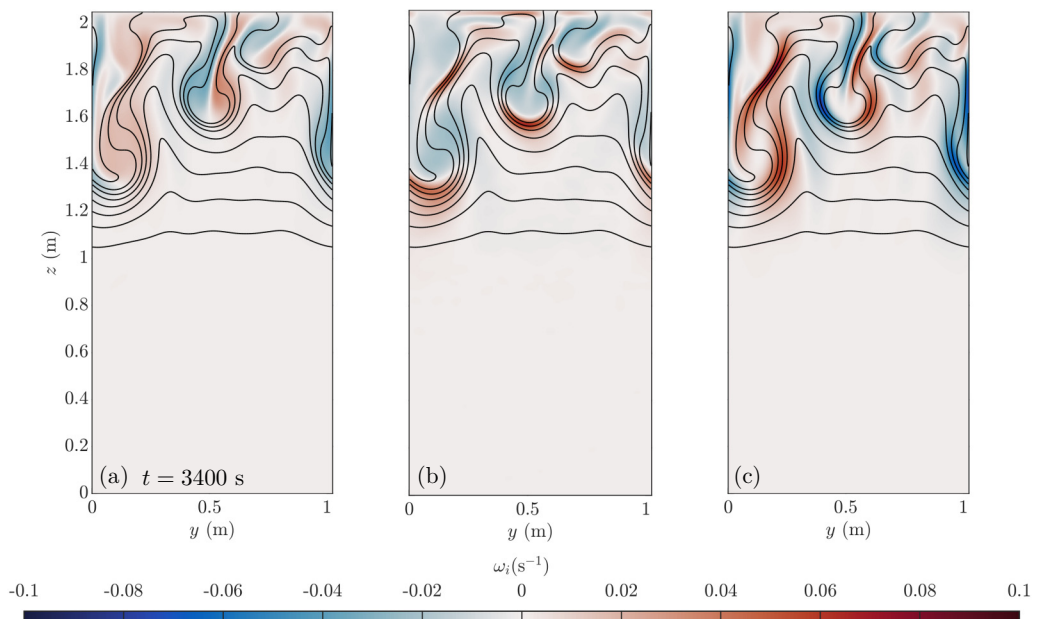
FIG. 8. Panels (a)–(c) show the y-z slices of each component of vorticity (x, y, and z respectively) at $t = 3400$ s for the Fast case. Contours of velocity are included on the plots.
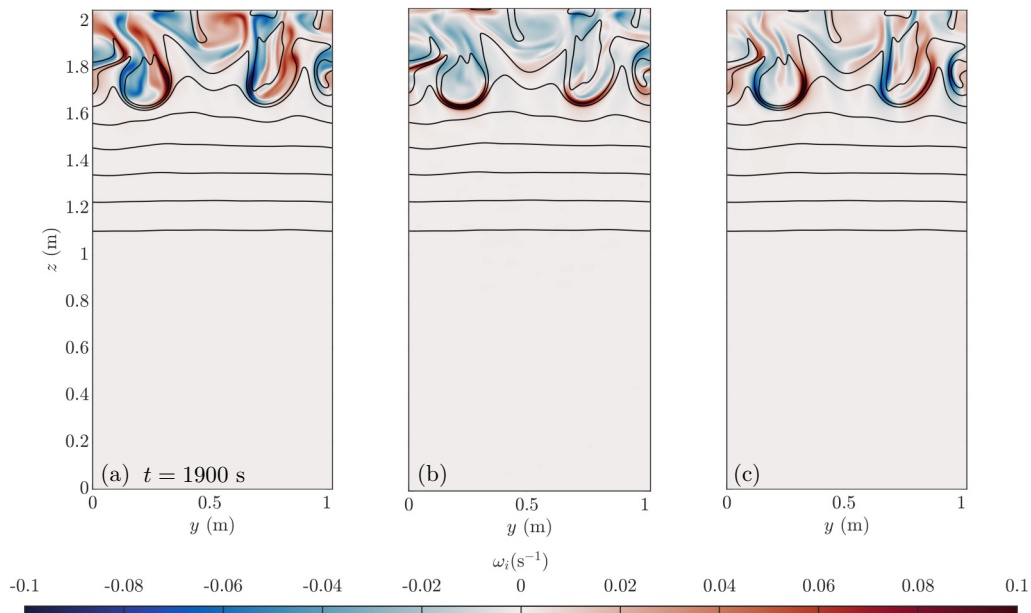
FIG. 9. Panels (a)–(c) show the y-z slices of each component of vorticity (x, y, and z respectively) at $t = 1900$ s for the Short-Attenuation case. Contours of velocity are included on the plots.

the spatial overlap of contours and large positive and negative vorticities. Generally speaking, the streamwise component of vorticity is a not a function of the streamwise component of velocity, and must be generated by spanwise variations in w or vertical variations in v. While there is some shear on fluid parcels caused by the falling plumes interacting with the upwelling water, the spanwise variations of w generated by this motion are small because the spatial variations of w are much smaller than variations in the other velocity components.

Shown in Fig. 9 are vorticity slices for the Short-Attenuation case at 1900 s. This time was chosen as it coincides with the first local minimum of $\tilde{\omega}_y^2$ for the Short-Attenuation case in Fig. 6. The same underlying principles can be seen to apply, except this time, the streamwise vorticity production is higher and more comparable to the spanwise and vertical. Since the shorter attenuation length implies a smaller length scale for the instabilities, the density and velocity gradients are potentially higher, leading to more vorticity production. Since the streamwise vorticity in the Short-Attenuation case becomes as active as the other two components sooner relative to the Fast case, the system goes unstable much earlier than the Fast case. The implication is that the smaller instabilities create thinner interfaces and higher resultant velocity gradients leading to enhanced streamwise vorticity production and to an earlier transition to turbulence.

Below we discuss the role that the vorticity dynamics plays in this process. To do this, first consider the terms that generate vorticity in the system, quantified by S_i and B_i.

Shown in Figs. 10(a) and 10(c) are profiles of S_i at $t = 3400s$ and $t = 3800$ s respectively for the Fast case. Figures 10(b) and 10(d) show the corresponding B_i values. The same quantities are shown for the Slow case in Fig. 11. The x, y, z components are given by the red, blue, and black curves. These times are shown because they describe the overall process that occurs during three-dimensionalization. For the Fast case, B_1 is systematically larger than S_1, but for the Slow case, S_1 and B_1 are generally comparable. This indicates that the generation of streamwise vorticity is primarily from baroclinic generation during the instability development phase in the Fast case whereas streamwise vorticity production is approximately the same from both mechanisms in the Slow case. At the same time, a comparison of S_2 and B_2 for the Fast case indicates that spanwise
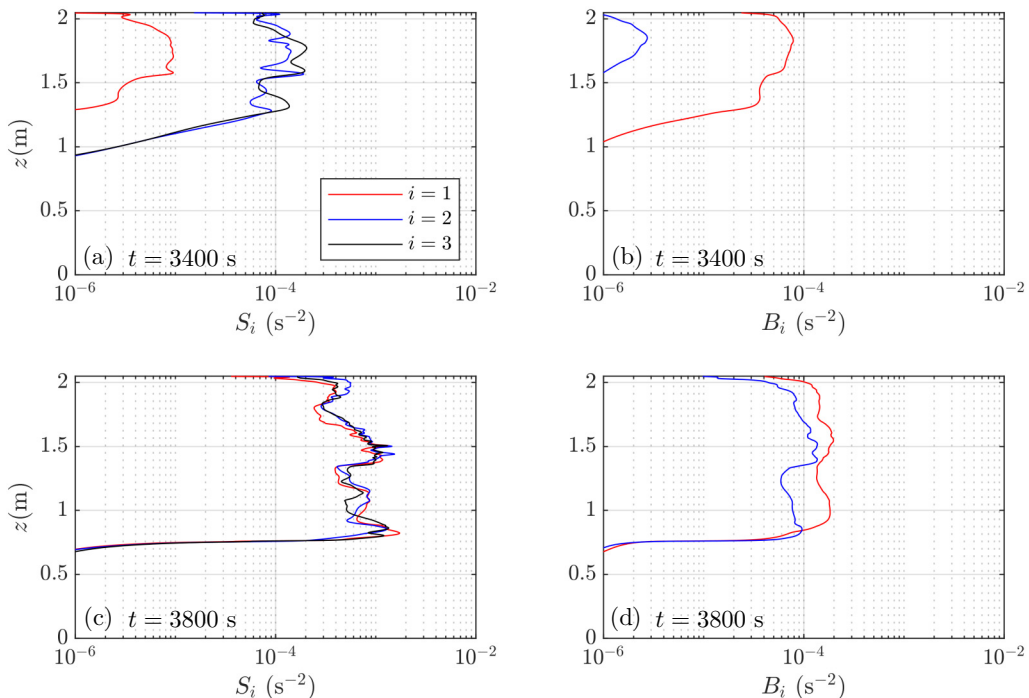
FIG. 10. (a) Profiles of the horizontal L^2 norm of each component of vortex tilting/stretching for the Fast case at $t = 3400$ s. (b) The horizontal L^2 norm of each component of the baroclinic vorticity production at $t = 3400$ s for the same case. (c, d) The same quantities but at $t = 3800$ s.

vorticity is generated primarily by vortex tilting/stretching as opposed to baroclinic production, while for the Slow case, these terms are of comparable magnitude again. This observation is consistent with the fact that there is very little streamwise variation in any variables at this time for the Fast case, where as the Slow case is fully three-dimensional. At a later time, during the three-dimensionalization of the Fast case we see that there is a substantial increase in S_1, S_2, and S_3 compared to the earlier time. Furthermore, the vorticity production coming from vortex tilting/stretching is greater than the baroclinic vorticity production by about an order of magnitude for both the spanwise and streamwise components. The baroclinic production is comparable across these two cases, while the production by tilting and stretching is greater in the Fast case. Thus, it is clear that it is vortex tilting/stretching that induces the three-dimensionalization, and not the baroclinic generation of vorticity.

The same premise follows for the Short-Attenuation and Short-Attenuation-Slow cases. Profiles of S_i and B_i for the Short-Attenuation case are shown in Fig. 12, while such profiles are omitted for the Short-Attenuation-Slow case, as they are very similar to Fig. 11, but concentrated near the surface. Note that the dimensional times are not equal across cases with different attenuation lengths because the transition happens earlier for cases with shorter attenuation lengths. However, qualitative comparisons can be made provided that the profiles are chosen just before the transition to three-dimensionalization. The key features to note here are the localization of the vorticity forcing near the surface, consistent with the smaller attenuation length and smaller instabilities, as well as the fact that the baroclinic generation of streamwise vorticity is much higher relative to the streamwise generation by tilting/stretching. This is consistent with higher density gradients induced by the smaller scale instabilities. This could explain the much larger streamwise component of vorticity when comparing Figs. 8 and 9.
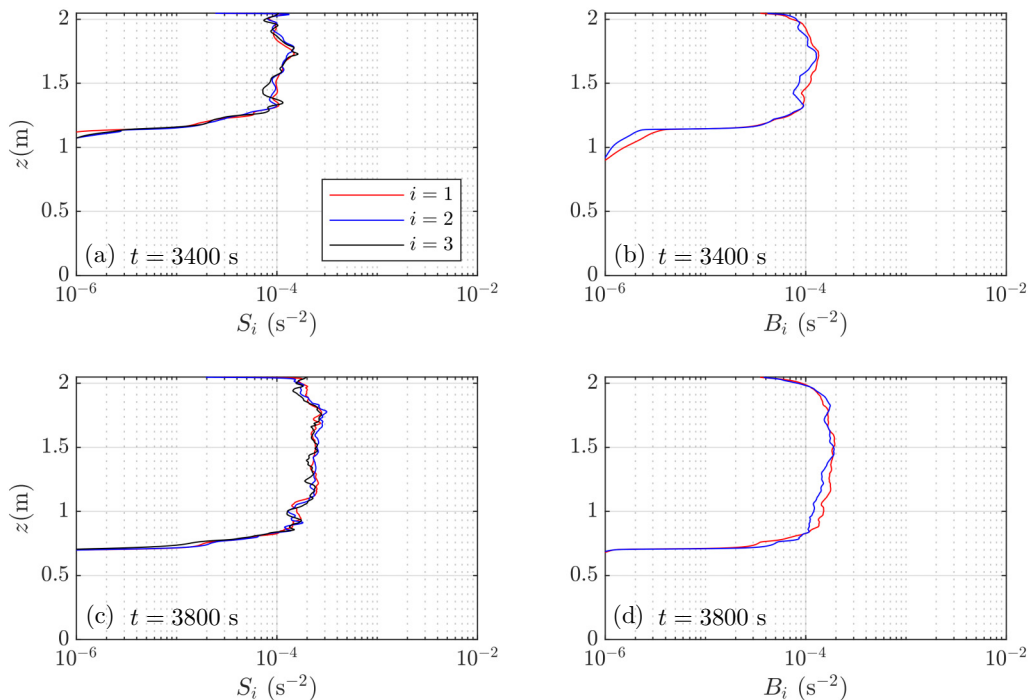
FIG. 11. As in Fig. 10 but for the Slow case.

VI. DISCUSSION

This paper presents three-dimensional simulations of cold water ($T < T_{md}$) convection induced by volumetric thermal forcing in the presence of a subsurface current in a horizontally periodic rectangular prism. In this temperature regime, density differences, characterized by the Atwood number, achieved within the flow are often much smaller than other studies citing low Atwood numbers [10–13]. The incident thermal forcing is a simplified model of solar radiation akin to Bouffard and Wüest [3], Ramón et al. [8], Ulloa et al. [9], and the background current is approximately linearly increasing from the mid-depth to the surface creating a region of constant shear and motionless region below. In this setup, heat is preferentially added to the near surface regions of the water column resulting in an unstable stratification, with the rate of attenuation of the incident radiation being controlled by ℓ.

Rayleigh-Taylor instabilities develop in all cases, but in cases with sufficiently strong shear, the background shear flow suppresses streamwise variation in the instabilities. The physical length scales of the instabilities that appear tend to correlate with the attenuation length. Cases with smaller attenuation lengths transition to a three-dimensional state earlier than cases with larger attenuation lengths.

All cases exhibited some degree of streamwise variability in the spatial structure of the instability but the variation was much stronger in the Base case and the Slow case. Whether or not the instabilities initially grow in a full three-dimensional state or a quasi-two-dimensional state is complicated by the fact that the background density profile is constantly changing. The criterion for determining if streamwise RTI will be suppressed [18] is rewritten here for convenience:

$$|U_z(z)| \geqslant \frac{\sigma_i}{\sqrt{2}}. \tag{19}$$
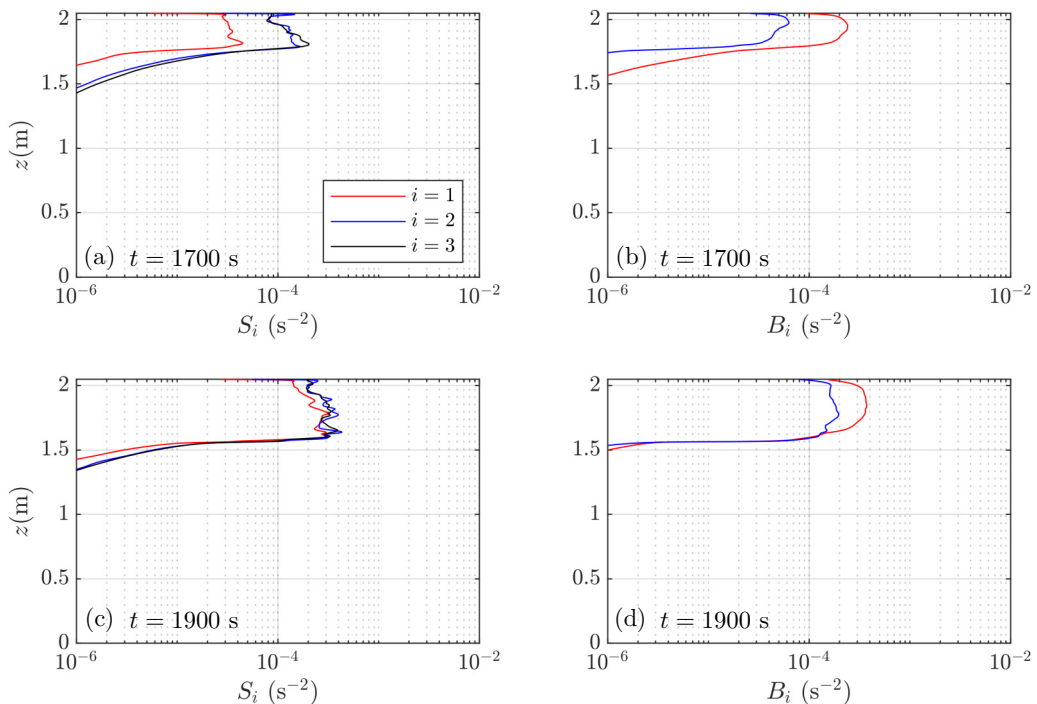
FIG. 12. (a) Profiles of the horizontal L^2 norm of each component of vortex tilting/stretching for the Short-Attenuation case at $t = 1700$ s. (b) The horizontal L^2 norm of each component of the baroclinic vorticity production at $t = 1700$ s for the same case. (c, d) The same quantities but at $t = 1900$ s.

Here $|U_z|$ is the local magnitude of the shear, and σ_i is the growth rate of the fastest growing instability in the absence of any background shear. In this setup, heat is continually added to the domain, and prior to instability formation, this heat modifies the stratification, which in turn modifies both the length scale of the fastest growing instability and the growth rate of instability. The background state in the Slow case quickly reaches a point where $\sigma_i/\sqrt{2} > |U_z|$, and this happens before significant modification of the background state and growth of the instability to its finite sized manifestation. Thus, when the perturbations finally grow, the shear that they experience is not strong enough to enforce the quasi-two-dimensional instability growth. Contrast this to the the Fast case, where the shear is ten times as strong, and instability occurs before $\sigma_i/\sqrt{2}$ becomes larger than $|U_z|$. Therefore, instabilities grow to finite amplitude in a quasi-two-dimensional state.

For large enough attenuation lengths (the Fast and Medium-Attenuation cases), the growth of the convective instabilities induces a vertical flux of streamwise momentum, rapidly increasing the spanwise and vertical components of vorticity [refer to Fig. 8(c)]. The rapid increase triggers three-dimensional tilting/stretching of vorticity, which finally allows the instabilities to go from a quasi-two-dimensional structure to a fully three-dimensional turbulent state. The Short-attenuation case exhibited qualitatively similar behavior [refer to Fig. 9(c)], but the baroclinic generation of vorticity was slightly stronger as the system transitioned from the quasi-two-dimensional state to the full three-dimensional one. The increased baroclinic production comes from the fact that the length scales between the plumes are much smaller in the Short-Attenuation case, allowing for higher horizontal density and velocity gradients leading to streamwise vorticity generation. This is evident in the fact that for the Short-Attenuation case, values of $\tilde{\omega}_x^2$ are higher than values of $\tilde{\omega}_z^2$ for much of the evolution.

The results of this study also bring up an important question about what one sees when simulating planar convection with a background shear flow. In many studies, planar convection is seen as a reasonable representation of the full three-dimensional physics, but by limiting the simulations to a single plane, the key mechanism responsible for three-dimensionalization and mixing is missing. When performing similar simulations to those in Table II, except limiting the domain to the x-z plane, the background shear flow completely stabilizes the upper portion of the water column. Convective heat fluxes are temporarily (and in some cases indefinitely) stopped within the domain, leading to a cooler lower layer relative to a run without a shear flow. The cases discussed in Benilov *et al.* [17] may suffer from this behavior, as there is no mechanism for the background state to become more unstable, thus eventually being able to overcome the stabilizing effects of the shear.

Building an understanding of the dynamical processes that are responsible for the transition from instability growth to turbulent convection in cold water is important for the eventual parametrization of these processes for larger-scale models. The heat added to the system generates upwelling and downwelling and an associated momentum transfer that in turn disrupts the background shear flow. As was shown in the Results section, the mechanism by which the system goes unstable was shown to be intimately linked to the presence of the shear flow. More research is needed to investigate the long term impact of the instability collapse and resultant turbulence on the background current. For example, once the system is in a turbulent state, is there some sort of equilibrium, or slowly varying but predictable background state that is achieved after enough time? Additionally, what does the turbulent state look like as the attenuation length is varied? In the limit of $\ell/H \to 0$, the system approaches a Rayleigh-Bénard type of convection system. Pirozzoli *et al.* [21] simulated the interaction of this form of convection with mean shear and identified robust streamwise rollers that increased the efficiency of the downward heat flux. Bouillaut *et al.* [33] used an experimental setup similar to the one presented in the present study. They heated a tank of freshwater from the bottom and measured the convective heat flux as a function of the Rayleigh number and ℓ/H and found that at larger ℓ/H, the upward heat flux was more efficient than for smaller values of ℓ/H, indicating that volumetric thermal forcing may be able to achieve the so-called "ultimate regime" of convection under the right conditions.

The results in this paper also highlight a gap in the understanding of turbulence generated by unstable stratification. As an example, consider the K-profile parameterization (KPP) Large *et al.* [36], a more modern review of which is found in Van Roekel *et al.* [37]. The KPP is a mixed layer model, with a term that parameterizes nonlocal turbulence based on boundary fluxes of heat and salt. Since radiation from the sun is a volumetric heating mechanism rather than a boundary flux, it is not clear how much solar radiation should be included in the nonlocal term [37], thus a separate parametrization for mixing in cold water by radiation may be needed. Furthermore, the parametrizations within the KPP are built on theories which rely on the presence of fully developed turbulence. It is interesting to note that the Reynolds numbers of the above simulations are quite low, indicating that the simulations may not reach a point where they could be considered as fully developed turbulence by models like the KPP. Low Reynolds numbers could indicate that the inertial sub-range of the kinetic energy spectra [31] where vortex tilting and stretching typically dominate, may not be fully formed. However, it is clear from Figs. 10–12 that stretching and tilting are still important to the development of the system.

Furthermore, future work should include a demonstration and discussion of the dynamics of a similar system where the background shear current is located near the bottom of the domain, as opposed to near the surface. This setup provides a companion to the simulations presented in this study. With a current located near the bottom, convective instabilities are free to form in three dimensions near the surface, and they can collapse and then contact the shear flow. Can the instabilities move momentum from the shear layer to the near surface region? Is this momentum flux more efficient once the instabilities collapse, or prior to collapse? Do fully three-dimensional instabilities become two-dimensional when they are subjected to the shear in this setup on long enough timescales?

Another direction one could consider is the impact of a different shear profile. One key feature that is ignored in this study is an inflection point in the background velocity profile. An inflection point is a necessary condition for the development of shear instabilities by Rayleigh's inflection point criterion [31]. Shear instabilities provide another mechanism to mix the water column [38], and depending on the strength of the shear, these shear instabilities may grow faster than any convective instabilities. Once in a turbulent mixed state, does the hypothetical system generated by shear instabilities differ from a turbulence point of view when compared to the system presented in this study?

APPENDIX A

The derivation for the Viscous Taylor Goldstein Equations can be found in Smyth *et al.* [35], and only the equations are presented below. k is the streamwise wave number, l is the spanwise wave number, and $\sigma = \sigma_r + i\sigma_i$ is the complex growth rate. Perturbations that have $\sigma_i > 0$ are unstable modes and grow without bound, and the growth rates of these modes are of general interest in this problem. The perturbation with the largest σ_i will grow the fastest, and the wave number of that mode sets the length scale of the instability that we see in the system. The equations are derived by substituting $\boldsymbol{u} = (U + u', v', w')$ and $\rho = \bar{\rho} + \rho'$ into the system of equations (2) - (4). Then, substitute the wave ansatz

$$(u', v', w', p', \rho') = (\hat{u}(z), \hat{v}(z), \hat{w}(z), \hat{p}(z), \hat{\rho}(z))e^{i(kx+ly-\sigma t)}. \tag{A1}$$

into the linearized system. Following this, define

$$\tilde{k} = \sqrt{k^2 + l^2}, \quad \tilde{\nabla}^2 = \frac{d^2}{dz^2} - \tilde{k}^2, \quad \tilde{U} = \frac{Uk}{\tilde{k}} \tag{A2}$$

and simplify. Then we get the following system of equations which govern the growth of perturbations to the system.

$$\sigma \tilde{\nabla}^2 \hat{w} = -i\tilde{k}\tilde{U}\tilde{\nabla}^2 \hat{w} + i\tilde{k}\tilde{U}_{zz}\hat{w} + \nu\tilde{\nabla}^4 \hat{w} - \frac{g}{\rho_0}\tilde{k}^2\hat{\rho}, \tag{A3}$$

$$\sigma \hat{\rho} = -\hat{w}\bar{\rho}_z - i\tilde{k}\tilde{U}\hat{\rho} + \kappa\tilde{\nabla}^2\hat{\rho}. \tag{A4}$$

APPENDIX B

Since the instabilities induce vertical fluxes of momentum, it is reasonable to expect some change in the mean profiles of velocity, since the current is incapable of being maintained by forcing or a pressure gradient. Shown in Fig. 13 are mean velocity profiles for the Fast (left) and Short-Attenuation (right) cases at three different times. The times are chosen are to highlight the state of the mean current before, during, and after the instability growth phase

For both cases, the key is that during the initial formation of the instability, the mean current becomes slightly modified by the growth of the instabilities, but there is still some evidence that the shear layer persists. However, once the instabilities have grown significantly, the shear layer structure has changed substantially. At this point, the instabilities have moved momentum from the
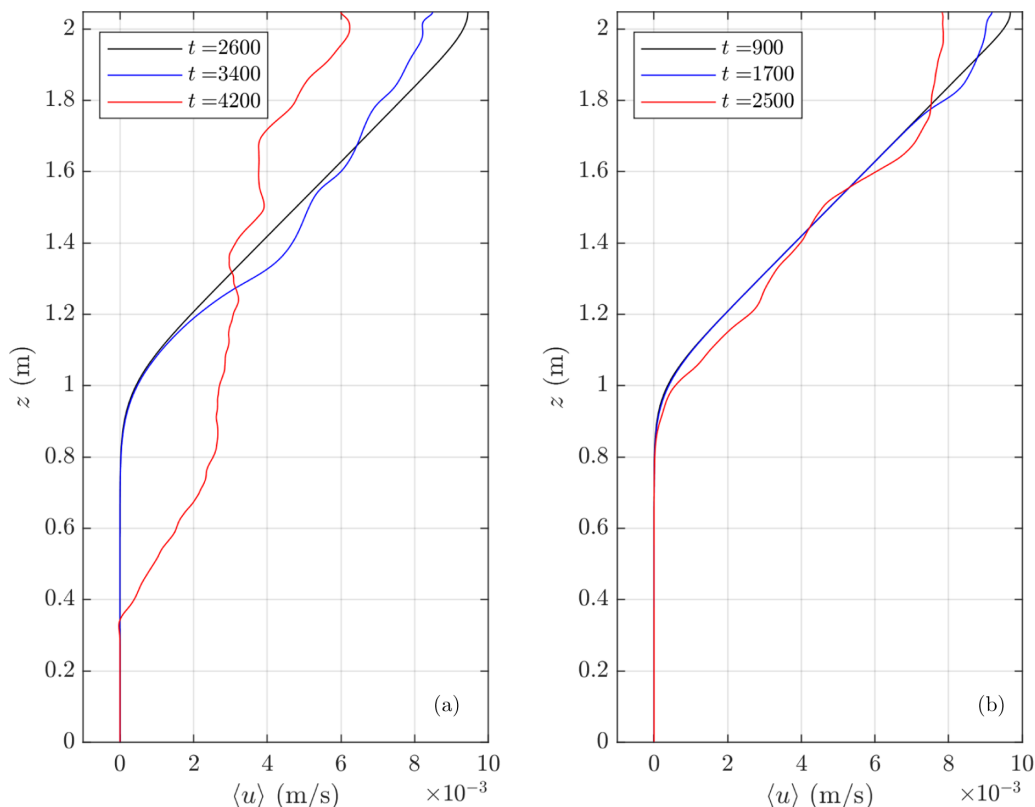
FIG. 13. Streamwise current profiles at three times for the Fast (a) and Short-Attenuation (b) cases. Times are chosen to highlight the mean streamwise current profile before instability formation (black), during the transition (blue), and in the three-dimensional state (red).

near surface regions to lower in the water column. The dimensional times that this process occurs is earlier for the Short-Attenuation case, consistent with the results described above.

[1] S. M. Powers and S. E. Hampton, Winter limnology as a new frontier, Limnol. Oceanogr. Bull. **25**, 103 (2016).

[2] J. Jansen, S. MacIntyre, D. C. Barrett, Y. Chin, A. Cortés, A. L. Forrest, A. R. Hrycik, R. Martin, B. C. McMeans, M. Rautio, and R. Schwefel, Winter limnology: How do hydrodynamics and biogeochemistry shape ecosystems under ice? J. Geophys. Res.: Biogeosci. **126**, 1 (2021).

[3] D. Bouffard and A. Wüest, Convection in lakes, Annu. Rev. Fluid Mech. **51**, 189 (2019).

[4] G. Kirillin, M. Leppäranta, A. Terzhevik, N. Granin, J. Bernhardt, C. Engelhardt, T. Efremova, S. Golosov, N. Palshin, P. Sherstyankin, G. Zdorovennova, and R. Zdorovennov, Physics of seasonally ice-covered lakes: A review, Aquat. Sci. **74**, 659 (2012).

[5] B. Yang, J. Young, L. Brown, and M. Wells, High-frequency observations of temperature and dissolved oxygen reveal under-ice convection in a large lake, Geophys. Res. Lett. **44**, 12,218 (2017).

[6] B. Yang, M. G. Wells, J. Li, and J. Young, Mixing, stratification, and plankton under lake-ice during winter in a large lake: Implications for spring dissolved oxygen levels, Limnol. Oceanogr. **65**, 2713 (2020).

[7] A. Cortés and S. MacIntyre, Mixing processes in small arctic lakes during spring, Limnol. Oceanogr. **65**, 260 (2020).

[8] C. L. Ramón, H. N. Ulloa, T. Doda, K. B. Winters, and D. Bouffard, Bathymetry and latitude modify lake warming under ice, J. Hydrol. Earth Syst. Sci. **25**, 1813 (2021).

[9] H. N. Ulloa, K. B. Winters, A. Wüest, and D. Bouffard, Differential heating drives downslope flows that accelerate mixed-layer warming in ice-covered waters, Geophys. Res. Lett. **46**, 13872 (2019).

[10] M. J. Andrews and S. B. Dalziel, Small Atwood number Rayleigh-Taylor experiments, Philos. Trans. R. Soc. A **368**, 1663 (2010).

[11] G. Boffetta, A. Mazzino, S. Musacchio, and L. Vozella, Kolmogorov scaling and intermittency in Rayleigh-Taylor turbulence, Phys. Rev. E **79**, 065301(R) (2009).

[12] G. Boffetta, A. Mazzino, S. Musacchio, and L. Vozella, Statistics of mixing in three-dimensional Rayleigh-Taylor turbulence at low Atwood number and Prandtl number one, Phys. Fluids **22**, 035109 (2010).

[13] B. Akula, M. J. Andrews, and D. Ranjan, Effect of shear on Rayleigh-Taylor mixing at small Atwood number, Phys. Rev. E **87**, 033013 (2013).

[14] J. Malm, L. Bengtsson, A. Terzhevik, P. Boyarinov, A. Glinsky, N. Palshin, and M. Petrov, Field study on currents in a shallow, ice-covered lake, Limnol. Oceanogr. **43**, 1669 (1998).

[15] J. L. Kasper and T. J. Weingartner, The spreading of a buoyant plume beneath a landfast ice cover, J. Phys. Oceanogr. **45**, 478 (2015).

[16] T. J. Weingartner, S. L. Danielson, R. A. Potter, J. H. Trefry, A. Mahoney, M. Savoie, C. Irvine, and L. Sousa, Circulation and water properties in the landfast ice zone of the Alaskan Beaufort Sea, Cont. Shelf Res. **148**, 185 (2017).

[17] E. S. Benilov, V. Naulin, and J. J. Rasmussen, Does a sheared flow stabilize inversely stratified fluid? Phys. Fluids **14**, 1674 (2002).

[18] V. S. Mikhailenko, E. E. Scime, and V. V. Mikhailenko, Stability of stratified flow with inhomogeneous shear, Phys. Rev. E **71**, 026306 (2005).

[19] H. L. Kuo, Perturbations of plane Couette flow in stratified fluid and origin of cloud streets, Phys. Fluids **6**, 195 (1963).

[20] F. Keisuke, N. Masamoto, and U. Hiromasa, Coherent structure of turbulent longitudinal vortices in unstably-stratified turbulent flow, Int. J. Heat Mass Transf. **34**, 2373 (1991).

[21] S. Pirozzoli, M. Bernardini, R. Verzicco, and P. Orlandi, Mixed convection in turbulent channels with unstable stratification, J. Fluid Mech. **821**, 482 (2017).

[22] C. J. Subich, K. G. Lamb, and M. Stastna, Simulation of the Navier-Stokes equations in three dimensions with a spectral collocation method, Int. J. Numer. Methods Fluids **73**, 103 (2013).

[23] T. J. McDougall, D. R. Jackett, D. G. Wright, and R. Feistel, Accurate and computationally efficient algorithms for potential temperature and density of seawater, J. Atmos. Ocean. Technol. **20**, 730 (2003).

[24] J. Olsthoorn, E. W. Tedford, and G. A. Lawrence, Diffused-interface Rayleigh-Taylor instability with a nonlinear equation of state, Phys. Rev. Fluids **4**, 094501 (2019).

[25] N. G. Jerlov, *Marine Optics* (Elsevier, Amsterdam, 1976), pp. 134–135.

[26] J. J. Simpson and T. D. Dickey, The relationship between downward irradiance and upper ocean structure, J. Phys. Oceanogr. **11**, 309 (1981).

[27] B. Hodges and C. Dallimore, Estuary, lake and coastal ocean model: ELCOM v2.2 Science manual, Centre for Water Research, University of Western Australia (2006).

[28] J.-M. Campin, P. Heimbach, M. Losch, G. Forget, A. Adcroft, D. Menemenlis, C. Hill, O. Jahn, J. Scott, M. Mazloff, E. Doddridge, I. Fenty, M. Bates, T. Martin, R. Abernathey, T. Smith, J. Lauderdale, B. Deremble, R. Dussin, P. Bourgault *et al.*, MITgcm User Manual (2019), https://mitgcm.readthedocs.io/en/latest/#.

[29] J. J. Simpson and T. D. Dickey, Alternative parameterizations of downward irradiance and their dynamical significance, J. Phys. Oceanogr. **11**, 876 (1981).

[30] A. Osadchiev, A. Barymova, R. Sedakov, R. Zhiba, and R. Dbar, Spatial structure, short-temporal variability, and dynamical features of small river plumes as observed by aerial drones: Case study of the Kodor and Bzyp river plumes, Remote Sens. **12**, 3079 (2020).

[31] P. K. Kundu and I. M. Cohen, *Fluid Mechanics*, 2nd ed. (Academic Press, San Diego, 1990).

[32] S. Grossmann and D. Lohse, Scaling in thermal convection: A unifying theory, J. Fluid Mech. **407**, 27 (2000).

[33] V. Bouillaut, S. Lepot, S. Aumaître, and B. Gallet, Transition to the ultimate regime in a radiatively driven convection experiment, J. Fluid Mech. **861**, R5 (2019).

[34] D. Bouffard, G. Zdorovennova, S. Bogdanov, T. Efremova, S. Lavanchy, N. Palshin, A. Terzhevik, L. R. Vinnå, S. Volkov, A. Wüest, R. Zdorovennov, and H. N. Ulloa, Under-ice convection dynamics in a boreal lake, Inland Waters **9**, 142 (2019).

[35] W. D. Smyth, J. N. Moum, and J. D. Nash, Narrowband oscillations in the upper equatorial ocean. Part II: Properties of shear instabilities, J. Phys. Oceanogr. **41**, 412 (2011).

[36] W. G. Large, J. C. McWilliams, and S. C. Doney, Oceanic vertical mixing: A review and a model with a nonlocal boundary layer parameterization, Rev. Geophys. **32**, 363 (1994).

[37] L. Van Roekel, A. J. Adcroft, G. Danabasoglu, S. M. Griffies, B. Kauffman, W. Large, M. Levy, B. G. Reichl, T. Ringler, and M. Schmidt, The KPP boundary layer scheme for the ocean: Revisiting its formulation and benchmarking one-dimensional simulations relative to LES, J. Adv. Model. Earth Syst. **10**, 2647 (2018).

[38] C. P. Caulfield, Mixing in turbulent stratified flows, Annu. Rev. Fluid Mech. **53**, 113 (2021).